crystals

MDPI

Article

Influence of Oxygen Vacancies on the Impedance Spectrum of Al_2O_3–$Na_{0.5}K_{0.5}NbO_3$ Composites

Alexander Martin [1,*], Kyle G. Webber [2] and Keni-chi Kakimoto [1]

[1] Department of Life Science and Applied Chemistry, Graduate School of Engineering, Nagoya Institute of Technology, Nagoya 466-8555, Japan
[2] Department of Materials Science and Engineering, Friedrich-Alexander-Universität Erlangen-Nürnberg (FAU), 91058 Erlangen, Germany
* Correspondence: martin.alexander@nitech.ac.jp

Abstract: Composites based on ferroelectric $Na_{0.5}K_{0.5}NbO_3$ (NKN) and paraelectric Al_2O_3 were observed using impedance spectroscopy at different temperatures. This allowed for the evaluation of the conduction processes of the bulk and grain boundary, revealing the occurrence of interdiffusion and changes in the conductive properties. The effective conductivity decreased with the increase in Al_2O_3, which is due to the highly resistive nature of Al_2O_3. Interestingly, the activation energy for the bulk response increased from 0.87 ± 0.06 eV to approximately 1.12 ± 0.03 eV, and the activation energy of the grain boundary decreased from 1.26 ± 0.09 eV to 0.99 ± 0.09 eV. These observations of the activation energy revealed the interdiffusion of Al^{3+} ions, leading to the formation of oxygen vacancies in close vicinity to the grain boundary. As a result, the conduction path for charge carriers shifted to take place predominantly along the grain boundary.

Keywords: impedance spectroscopy; composites; lead-free ferroelectrics

check for updates

Citation: Martin, A.; Webber, K.G.; Kakimoto, K.-c. Influence of Oxygen Vacancies on the Impedance Spectrum of Al_2O_3–$Na_{0.5}K_{0.5}NbO_3$ Composites. *Crystals* **2023**, *13*, 463. https://doi.org/10.3390/cryst13030463

Academic Editor: Haibo Zhang

Received: 3 February 2023
Revised: 26 February 2023
Accepted: 3 March 2023
Published: 8 March 2023

1. Introduction

Piezoceramics based on lead-free $Na_{0.5}K_{0.5}NbO_3$ (NKN) are very promising environmentally friendly materials for high-temperature applications due to their high Curie points [1,2]. Furthermore, among piezoelectric properties, the piezoelectric charge coefficient d_{33} can reach values between 350 and 650 pC/N, similar to common lead zirconate titanate (PZT) compositions [1,2]. To further increase important values for sensor [3,4] or actuator applications [4,5], composites are a viable option. Therefore, the concept of ceramic/ceramic composites for energy-harvesting applications was explored using the model material NKN + 0.2% MnO/Al_2O_3 in a recent study [6]. Despite the decrease in the piezoelectric properties, the generated power density remained approximately 0.1 $\mu W/mm^3$ between 0 and 15 vol% Al_2O_3 [6]. As a result, this approach might be interesting for the optimization of piezoelectric energy harvesters. In addition, the composite approach was used to improve several other aspects of NKN-based ceramics. For instance, Yu et al. observed increased thermal stability in hot-pressed NKN with the addition of 0.5 mol% Al_2O_3 compared to pure NKN ceramics [7]. Furthermore, NKN/Al_2O_3 composites were manufactured with the aim to improve upon the microwave absorption properties [8,9]. Other piezoelectric materials have been modified with the addition of Al_2O_3 as secondary particles, as well. Thommerel et al. modified the resonance frequency of $Pb_{0.925}La_{0.05}$ $(Zr_{0.53}Ti_{0.47})O_{3-\delta}$ ceramics [10], allowing for the adjustment of said frequency according to the application. Cao et al. induced a metastable ferroelectric phase into $Pb_{0.99}Nb_{0.02}$ $[(Zr_{0.57}Sn_{0.43})_{0.94}Ti_{0.06}]_{0.98}O_3$ ceramics via internal stress caused by the thermal expansion mismatch with Al_2O_3 particles [11]. This metastable phase led to an increase in the pyroelectric response. However, during the sintering process, interdiffusion can occur, leading to an interface with different properties, which in turn can change the macroscopic properties. This can be seen in studies that directly substituted the A or B atoms of the perovskite crystal structure in NKN-based materials.

The inclusion of Li^+ ions in the crystal structure leads to an increase in the piezoelectric properties, such as d_{33} (>200 pC/N) and k_p (>40%) [12], which is understood to be due to the shift of the polymorphic phase temperature to room temperature. Furthermore, Tan et al. have shown that the substitution of Al in $0.955(K_{0.5}Na_{0.5})(Nb_{0.965}Sb_{0.035})O_3$-$0.045(Bi_{1-x}Al_x)Na_{0.5}ZrO_3$ ceramics leads to a piezoelectric charge coefficient of approximately 570 pC/N [13]. After adding ZrO_2 or TiO_2, Vendrell et al. observed an increase in the piezoelectric charge coefficient from approximately 110 pC/N to 134 pC/N and 124 pC/N, respectively [14]. This was ascribed to the increased number of oxygen vacancies introduced via acceptor doping. Furthermore, by optimizing the number of oxygen vacancies, electric-field-induced strains can be enhanced [15]. This was shown by Zhao et al., who introduced Fe^{2+} and Cu^+ ions into the lattice of NKN, revealing a unipolar strain of approximately 0.5% at 5 kV/mm, achieved through the formation of defect dipoles and internal bias fields [15]. On the other hand, studies on $BaTiO_3$ have shown that an increased concentration of oxygen vacancies can induce time-dependent degradation, which could be mitigated by co-doping with donor materials [16]. Similar changes in the electromechanical properties are expected in the case of composites around the particles, where, through substitution, an interface occurs. To gain a better understanding of this interface, we focus on changes in the electrical properties, mainly impedance, using impedance spectroscopy.

Impedance spectroscopy is a versatile tool that can be used to characterize the electrical properties of polycrystalline microstructures [17]. In addition to the possibility of gathering information on the dielectric and conductive properties of grains, grain boundaries, and interfaces, changes in the domain structure and oxygen vacancies can be measured [18–21]. For instance, Zeng et al. showed that the activation energy evaluated by the temperature-dependent conductivity could be decreased by doping $0.3Pb(Zn_{1/3}Nb_{2/3})O_3$–$0.7Pb(Zr_{0.49}Ti_{0.51})O_3$ with LiF, as the number of oxygen vacancies increased [18]. Similar results were measured for Tb- and Tm-doped NKN [19]. However, the activation energy can also be changed during fatigue, as shown by Nishiyama et al. [20] in Li-modified NKN. Here, the changes were attributed to the anisotropic character of the ion conductivity of the lattice; due to an increase in the c-axis orientation along the measurement direction during fatigue, the ion conductivity increased macroscopically. On the other hand, in the material system $(K_{0.5}Na_{0.5})(Nb_{0.995}Mn_{0.005})O_3$–xCuO ($0 \leq x \leq 2$ mol%), an increase in the activation energy was observed [21], suggesting either a decrease in oxygen vacancies or overall lower ion conduction. Therefore, impedance spectroscopy can give information not only about the conductivity of a material but also potentially about the concentration of oxygen vacancies.

As impedance spectroscopy allows for the distinction between grains and grain boundaries, it is used to measure the contribution to the overall impedance of these different aspects of a polycrystalline sample. As a result, by knowing each contribution to the dielectric and electric properties, composites can be optimized to achieve favorable properties. As such, impedance spectroscopy has been used to analyze 3-0 composite piezoelectrics (notation after Newnham [22]). For instance, in order to achieve the magnetoelectric effect, $Ni_{0.5}Zn_{0.5}Fe_2O_4$ [23] and $CoFe_2O_4$ [24] were added to PZT. In the first case, impedance spectroscopy revealed the main contribution to the overall resistivity to stem from the grain boundary due to the formation of a glass phase [23], whereas in the $Pb_{0.52}Zr_{0.48}TiO_3$–$CoFe_2O_4$ composites, the oxide-ion conductor phase of $Pb_{0.52}Zr_{0.48}TiO_3$ and the polaronic conductor phase of $CoFe_2O_4$ [24] showed separate relaxation responses. As such, impedance spectroscopy was used in this study in order to reveal the different contributions of the grain and grain boundary in the previously reported ferroelectric NKN + 0.2% MnO/paraelectric Al_2O_3 composites. Furthermore, the impact of the interface on the electric properties was observed. Additionally, activation energies were determined, thus giving an idea of the concentration of oxygen vacancies. These results were then used to clarify to what extent interdiffusion between materials occurred.

2. Materials and Methods

2.1. Sample Preparation

$Na_{0.55}K_{0.45}NbO_3$ doped with 0.2 mol% MnO was synthesized via the mixed-oxide method. Hereafter, this composition will be referred to as NKN. Starting powders of K_2CO_3, Na_2CO_3, and Nb_2O_5 (all with a purity of 99.9%, Rare Metallic, Japan) were stoichiometrically weighed and mixed. The raw powders were wet-milled for 16 h with ZrO_2 ball media (5 mm diameter) in anhydrous acetone. After ball milling, the powders were calcined at 910 °C for 10 h in air, followed by a second milling step for 16 h. Subsequently, varying amounts of Al_2O_3 powder (purity of 99.99%; Rare Metallic, Japan; average particle size: 0.55 µm, with a standard deviation of 0.43 µm) were added. As a result, 6 different compositions were produced with 0, 5, 10, 15, 20, and 25 vol% Al_2O_3. Spark plasma sintering (SPS) was used to densify the samples at 1000 °C for 10 min under 80 MPa uniaxial pressure. After a subsequent annealing step at 950 °C for 10 h in air, the samples were ground using SiC grinding papers of varying grades to a thickness and diameter of approximately 700 µm and 10 mm, respectively. Relative densities above 95% were measured for each sample using the Archimedes method. The average grain sizes were approximately 0.70 µm, 0.78 µm, 0.59 µm, 0.56 µm, 0.65 µm, and 0.57 µm in the NKN samples with the addition of 0 vol%, 5 vol%, 10 vol%, 15 vol%, 20 vol%, and 25 vol% Al_2O_3, respectively. More detailed information about the samples can be found elsewhere [6]. The cylindrical surfaces were coated with a silver paste and annealed at 700 °C for 5 min, which solidified the electrode but also reduced residual stresses, which might have been introduced during the grinding step.

2.2. Sample Characterization

Relative permittivity and dielectric loss were measured from 360 to 450 °C with an LCR meter (ZM 2355, NF Corporation, Japan), which was connected to a tube furnace (KTF035N, Koyo Thermo Systems, Japan). During measurement, the heating rate was 3 °C/min. The measurement frequency was 1 kHz, and the amplitude of the applied AC voltage was ±5 V.

Impedance spectra between 50 mHz and 250 kHz were collected using a frequency response analyzer (FRA5097, NF Corporation, Japan) connected to a current amplifier (CA5350, NF Corporation, Japan). The spectra were gathered in 10 °C intervals between temperatures of 360 °C and 450 °C. The alternating voltage amplitude was adjusted depending on the sample thickness in order to apply a fixed electric field of 0.5 V/mm to each sample. Impedance probes the entire volume of the sample, averaging numerous grains and grain boundaries. This, therefore, requires modeling to analyze the averaged data. As the grain size is relatively homogeneous throughout each sample, a model was used [25], and the obtained impedance spectra were fitted using the software As-510Z (NF Corporation, Japan). In order to fit the data, an equivalent circuit with two parallel circuits, consisting of a resistor and a constant phase element (CPE), was used. These two circuits represent the response of the bulk and grain boundaries. The impedance Z_{CPE} of these R-CPE circuits can be calculated as a function of frequency ω by using resistance R, the CPE constant T_{CPE}, and the CPE index p:

$$Z_{CPE} = \frac{R}{1 + (j \cdot \omega)^p T_{CPE} \cdot R} \tag{1}$$

In addition, the capacitance C, as well as the relaxation frequency of each circuit, can be calculated using Equations (2) and (3), respectively.

$$C = T_{CPE}{}^{\frac{1}{p}} \cdot R^{\frac{1-p}{p}} \tag{2}$$

$$f_{max} = \frac{1}{2\pi (T_{CPE} \cdot R)^{\frac{1}{p}}} \tag{3}$$

Since the conductive and dielectric properties of a material vary with frequency, it is necessary to use complex expressions for the impedance (Z^*) and electric modulus (M^*). The real (Z', M') and imaginary (Z'', M'') parts of these complex parameters are related to each other as follows:

$$Z^* = Z' + jZ'' \tag{4}$$

$$M^* = M' + jM'' = j\omega C_0 Z^* \tag{5}$$

Where required, data points were fitted using the built-in linear fitting function in IgorPro 8 (Wavemetrics, Portland, OR, USA).

3. Results

The impedance of the composite material is affected by its conductive and dielectric properties. As such, Figure 1 displays the relative permittivity and dielectric loss of NKN with different vol% Al_2O_3 as a function of temperature. At approximately 400 °C, an anomaly was observed, which is understood to be the Curie point of NKN separating the ferroelectric tetragonal (*P*4*mm*) and paraelectric cubic (*Pm*3*m*) phases [26]. An overall decreasing trend of permittivity with increasing amounts of paraelectric Al_2O_3 was apparent, as well as a decrease in the Curie point. This is in line with previous findings, where hot-pressed NKN with the addition of 0.5 mol% Al_2O_3 exhibited a slight decrease in the Curie point after calcination [7]. In addition, Fisher et al. have shown that with an increasingly more reducing atmosphere, the Curie point shifts to lower values [27]. These changes were attributed to an increase in the concentration of oxygen vacancies. In other ferroelectric materials, such as $BaTiO_3$, a decrease in the Curie point is observed when Fe [28] is introduced into the perovskite lattice. The decrease in this study could therefore stem from the interdiffusion of Al^{3+} ions. Cheng et al., on the other hand, found that substituting the B-side of the perovskite structure with Al^{3+} leads to an increase in the Curie point [29]. It should be noted that, here, significant differences in the microstructure were apparent, which was shown to have an effect on the phase transition temperature [30]. In NKN ceramics, an increase in grain size leads to an increase in the Curie point [30]. Since there was a slight decrease in the average grain size in this study, this could have potentially had another impact on the phase transition temperature. Furthermore, a decreasing effect has been previously observed in other perovskite ferroelectrics, such as $BaTiO_3$ [31,32], during the application of external hydrostatic pressure. It should be noted that the direction of the shift depends on the kind of applied mechanical stress. For instance, it was previously shown that uniaxial compressive stress increased the Curie point of NKN-based ceramics [33]. As such, the stress state in the composites is suggested to be of a hydrostatic nature, leading to a shift of the phase transition temperature to lower values.

On the other hand, the dielectric loss showed an increasing trend with a subsequent decrease, reaching a minimum of 0.2 at 360 °C for NKN with 25 vol% Al_2O_3. It is possible that the introduction of Al_2O_3 results in two opposing effects that increase and decrease the dielectric loss. The introduction of Al_2O_3 should theoretically decrease the dielectric loss, since alumina has a significantly lower value than NKN [34]. Nevertheless, interdiffusion between the two materials during the sintering process is unavoidable, which leads to an interface with potentially higher dielectric loss. As such, the latter effect is more pronounced at 5 vol% but is taken over by the first with increasing amounts of Al_2O_3. It should be noted that sample variations in the microstructure and porosity could lead to differences, as well.

Besides the shift of the Curie point, the Curie–Weiss temperature and the diffusiveness of the phase transition can change with the introduction of stress or dopants [28,32,35,36]. In the paraelectric phase, the temperature dependence of the dielectric constant of NKN is described by the Curie–Weiss law. The Curie–Weiss temperature θ was determined by performing a linear extrapolation of the inverse dielectric constant from the high-temperature region to zero. The Curie point and Curie–Weiss temperature are shown in Figure 1b as a function of vol% Al_2O_3. The difference between T_C and θ increased with the addition of 5 vol% Al_2O_3 and remained relatively constant with additional amounts.

This suggests an increase in the first-order character of the transition, which can also be observed as a decrease in the maximum permittivity [32]. This would be consistent with the mechanism of uniaxial compression [35]. However, due to a decrease in the Curie point, hydrostatic compression was suggested, which would lead to a phase transition of the second order, meaning that the Curie point and Curie–Weiss temperature coincide [37]. On the other hand, $BaTiO_3$ showed a general increase in the difference between T_C and θ with increasing amounts of the dopant [28]. Only at higher amounts was a decreasing trend observed, which would be consistent with the results of this study.

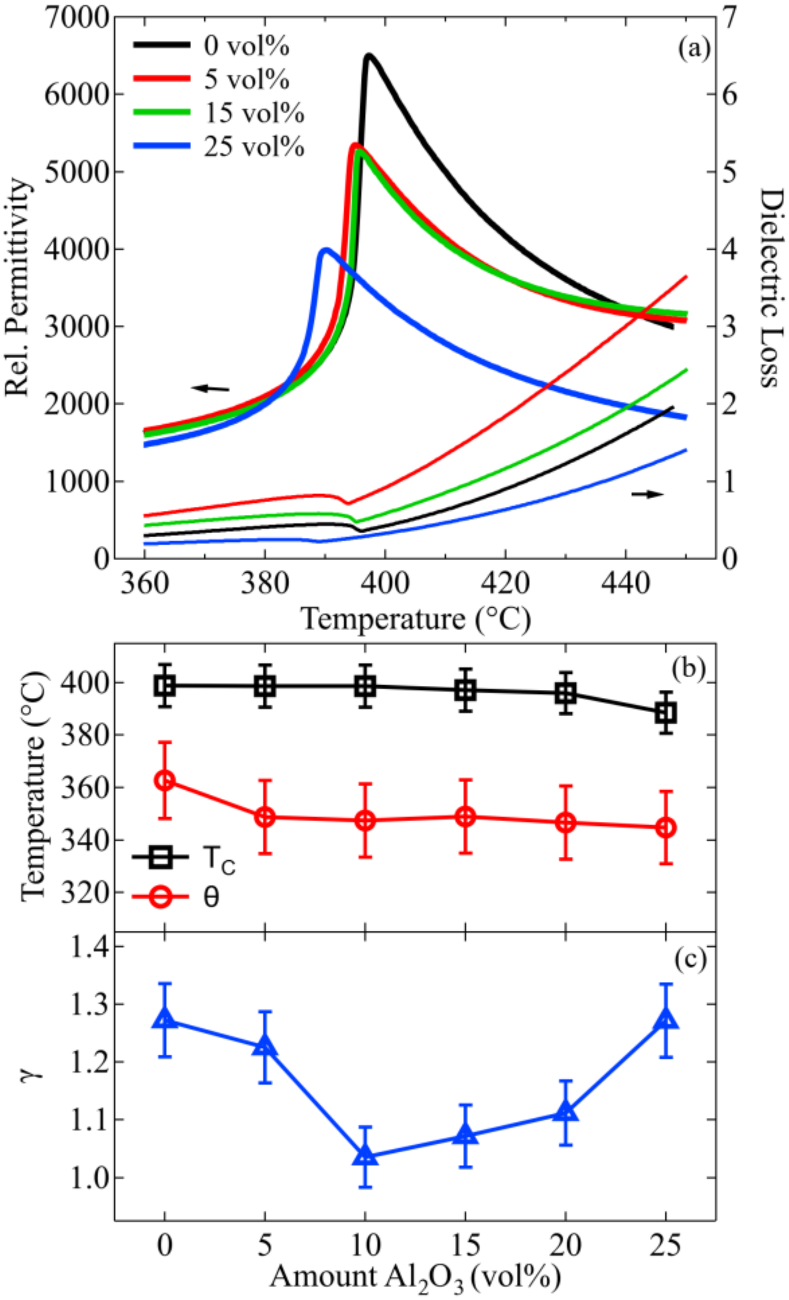

Figure 1. Relative permittivity and dielectric loss between 360 °C and 450 °C for NKN with specific vol% Al_2O_3 (**a**). Shift of Curie point and Curie–Weiss temperature (**b**) and measured exponent γ in Equation (7) (**c**) of NKN as a function of vol% Al_2O_3.

In order to determine the diffusiveness of the phase transition, Uchino and Nomura proposed an empirical relation [36]:

$$\frac{1}{\varepsilon'} - \frac{1}{\varepsilon_m} = \frac{(T - T_m)^{\gamma}}{K} \tag{6}$$

where ε_m is the maximum permittivity, T_m is the corresponding temperature, and K is a constant. The exponent γ is used to characterize the diffusiveness of the phase transition, where a value of $\gamma = 1$ represents a sharp transition, and a value $\gamma = 2$ corresponds to a diffuse transition. The value of γ was determined by performing linear regression fits to log–log plots of permittivity as a function of temperature, as described in Equation 6. The obtained values are shown in Figure 1c as a function of vol% Al_2O_3. The diffusiveness of the phase transition decreased from approximately 1.3 to 1.1 between 0 and 10 vol%. After plateauing between 10 and 20 vol%, the exponent increases again to approximately 1.25. This trend is consistent with previous studies on $BaTiO_3$ and Fe as a dopant [28]. Mechanical stress, on the other hand, would show an overall increasing character in diffusiveness [35]. As such, the results point toward the interdiffusion of Al^{3+} ions being the predominant process at lower vol% Al_2O_3. Due to the concurrent effects of internal stress, interdiffusion, and doping at higher Al_2O_3 contents, the exact mechanism driving the observed trend remains uncertain. In order to better understand the sample-to-sample variation in one composition, three samples were measured in total for each vol% Al_2O_3. To have a conservative estimate of the variation, the largest standard deviation was chosen, with the added uncertainty from the linear fitting function. This resulted in variations of ±2%, ±4%, and ±5%, for the Curie point, Curie–Weiss temperature, and diffusiveness, respectively. The possible reasons for the variation are as follows: firstly, the estimation of the Curie–Weiss temperature and diffusiveness rely on the estimation of said values via the fitting function; secondly, the observed variance between the samples could also be related to the microstructure, since grain size and porosity affect the diffusiveness of the phase transition. For instance, decreasing the grain size increases the diffusiveness [38–40]. Additionally, the aforementioned interdiffusion between the materials is dependent on the connection between the NKN and Al_2O_3 particles during the sintering process. The agglomeration of Al_2O_3 could still be present, with the variation in the amount resulting in different volumes of the interface between the two materials. As previously discussed, oxygen vacancies can change the Curie point, as well as the Curie–Weiss temperature and diffusiveness. Furthermore, due to differences in the thermal expansion coefficient, mechanical stress can occur during and after the sintering process. Variations in this internal stress can lead to variations between samples of the same composition, since mechanical stress has been shown to impact the discussed values in Figure 1b,c.

Figure 2 shows the frequency-dependent imaginary versus real part of the impedance (Nyquist plots) of the prepared composites with different Al_2O_3 contents as a function of temperature. All samples exhibit two semicircles that refer to the high- and intermediate-frequency-associated bulk and grain boundary impedance, respectively [17,41], where the low-frequency tail feature of the impedance spectra appears due to the electrode/material interface. As the temperature increases, the radius of the two semicircles decreases, which is likely due to an increase in the overall conductivity. Between 410 °C and 420 °C, the temperature range at which NKN transitions from a ferroelectric tetragonal phase into a paraelectric cubic phase, a significant decrease in real and imaginary impedance occurred. With increasing amounts of Al_2O_3, the response evolves into a single semi-circle due to the superimposed bulk and grain boundary contributions. Furthermore, it should be noted that the range of the *y*-axis, as well as the *x*-axis, is adjusted for different Al_2O_3 contents to improve visibility. As such, when comparing the different compositions, an increase in the real and imaginary impedance with increasing vol% Al_2O_3 is apparent. Similar to what has been observed in $Pb_{0.925}La_{0.05}$ $(Zr_{0.53}Ti_{0.47})O_{3-\delta}$ with variable fractions of Al_2O_3 [10], the change could be due to an increase in the resistivity of the bulk response with increasing content.

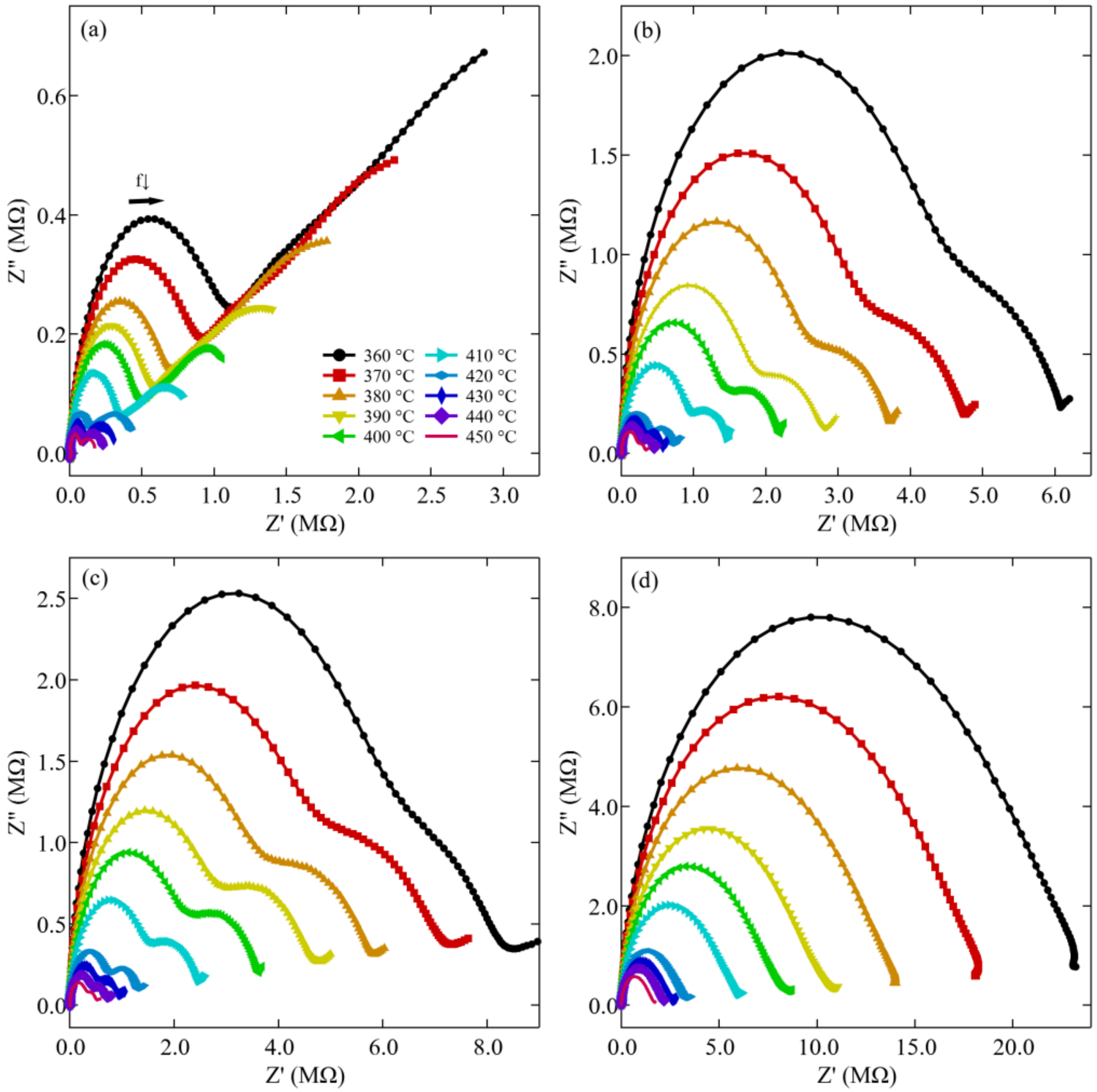

Figure 2. Nyquist plots of NKN with (**a**) 0 vol%, (**b**) 5 vol%, (**c**) 15 vol%, and (**d**) 25 vol% Al_2O_3.

To gain more insight, the imaginary part of the impedance (Bode plot), as well as the electrical modulus, is shown as a function of frequency (Figure 3). Similar to the Nyquist plots discussed earlier, two relaxation processes can be observed for all composites for the Bode plots. At 360 °C, the relaxation frequency for the bulk material is in the range of 0.1–1 kHz. At lower frequencies, around 10 Hz, the relaxation process for the grain boundary can be observed. In general, the relaxation frequencies of a material depend on the conductivity σ, as well as on the relative permittivity ε_r:

$$2\pi f = \frac{\sigma}{\varepsilon_0 \varepsilon_r} \tag{7}$$

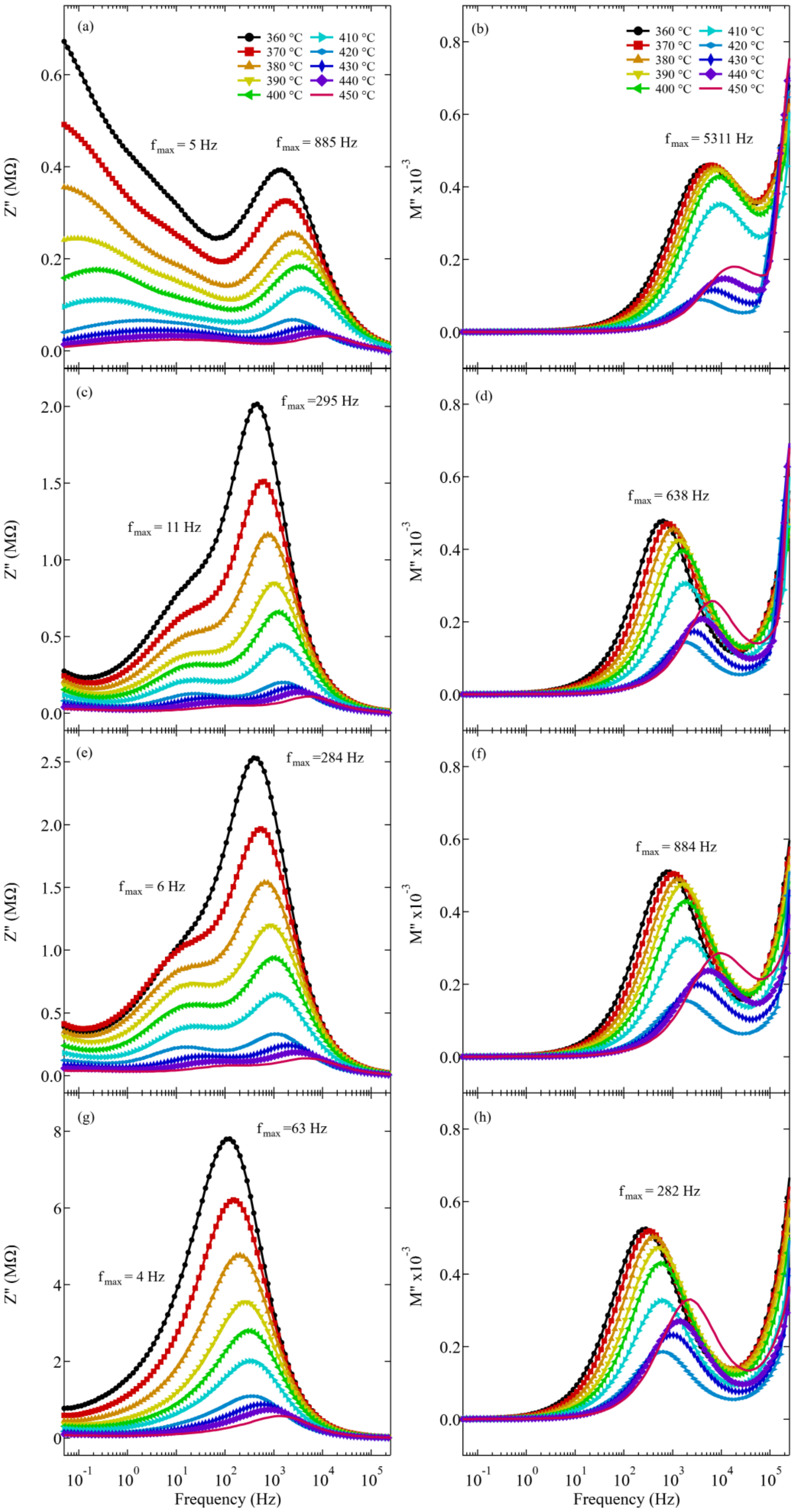

Figure 3. Imaginary part of the impedance and electrical modulus of NKN with (**a**,**b**) 0 vol%, (**c**,**d**) 5 vol%, (**e**,**f**) 15 vol%, and (**g**,**h**) 25 vol% Al_2O_3 as a function of frequency.

With increasing temperature, both maxima shift to higher frequencies, which is likely due to an increase in conductivity, suggesting that the bulk and grain boundary relaxation process is thermally activated. On the other hand, the relaxation frequency of the bulk response decreases with increasing amounts of Al_2O_3. Interestingly, the response of the grain boundary remains relatively constant. In order to understand this behavior, additional factors that may influence the relaxation frequency will be discussed. For instance, the decreasing trend in the relaxation frequency of the bulk may indicate a decrease in conductivity rather than changes in capacitance. At 360 °C the relative permittivities were 1526, 1540, 1495, 1372, and 1369 for NKN samples with 0 vol%, 5 vol%, 10 vol%, 15 vol%, 20 vol%, and 25 vol% Al_2O_3, respectively. With decreasing permittivity, the relaxation frequencies would shift to higher values, indicating that conductivity is the predominant factor. Another aspect that can change the value of the relaxation frequency is the change in the microstructure. This was shown for $0.925(K_{0.5}Na_{0.5})NbO_3 0.075Bi(Zn_{2/3}(Ta_{0.5}Nb_{0.5})_{1/3})O_3$ ceramics, where the bulk resistance gradually increased with decreasing grain size [42]. Since the average grain size did decrease with increasing vol% Al_2O_3 [6], a similar trend is to be expected. However, it should also be noted that the microstructure remained in relatively the same order of magnitude, suggesting a rather small impact [6]. Furthermore, the electrical insulative property of Al_2O_3 would have an effect analogous to that of pores. Previous studies have shown that the effective conductivity decreases with increasing porosity, resulting in a shift to lower frequencies [43]. A similar effect should therefore be observed not only for the bulk but also for the grain boundary response. The last possibility is that, through interdiffusion, Al_2O_3 changes the conductivity of the grain boundary/creates an interface with different conductivities. This has been observed for YSZ/Al_2O_3 composites, where the interface had a higher conductivity, thus increasing the relaxation frequency [44,45]. Interestingly, a slight increase in the relaxation frequency was observed between 0 and 5 vol%. Similar observations were made on YSZ/Al_2O_3, where the grain boundary conductivity increased between 0 and 1 wt%, followed by a gradual decrease with the further addition of Al_2O_3 [44]. It is likely that the pore effect and the formation of the interface have opposing effects on conductivity. Whereas the formation of the interface decreases the conductivity of the grain boundary, the addition of Al_2O_3 decreases the overall conductivity for both bulk and grain boundary.

To further confirm this, the electric modulus M was calculated, since changes in the modulus suggest possible changes in capacitance, whereas changes in the impedance are based on changes in resistance [46]. The electric modulus was calculated from Equations (4) and (5). From the values of M^*, the imaginary part was determined. Maxima were clearly observed to be similar to the peaks in the impedance representing dielectric relaxation processes, albeit at different frequencies. In the ideal Debye-type relaxation process, the two peaks should coincide at the same frequency [47]. The large full width at half maximum and the asymmetrical shape of the peaks also suggest non-Debye behavior [48]. Similar to the observations on the relaxation peaks of the impedance, the maxima shifted to the higher frequency range with an increase in temperature, further confirming that the relaxation process is a thermally activated process. In addition, the value decreases with temperature until reaching the Curie point. Afterward, the peak increases in value with increasing temperature. The peak maxima are related to the relative permittivity as follows:

$$M''_{max} = \frac{1}{2\varepsilon_r} \tag{8}$$

Since NKN undergoes a first-order ferroelectric-to-paraelectric phase change, the permittivity exhibits a finite maximum, and the electric modulus shows a minimum. Furthermore, since the maximum was only observed for the grain, it can be concluded that the dielectric relaxation is derived from the grain response. The increasing value of the peak maximum can also be explained by the actuation of the small polaron hopping mechanism and a simultaneous decrease in electron–lattice coupling, which was observed in a previous study on $(Na_{0.52}K_{0.4425}Li_{0.0375})(Nb_{0.92}Ta_{0.08})O_3$ to be well above the Curie point [49]. With increasing Al_2O_3 concentrations, the relaxation peak shifts to lower frequencies, which suggests an increase in the relaxation time that is closely related to a decrease in dielectric permittivity (Figure 1). This is further confirmed by the increase in the maximum values of M'' with increasing amounts of Al_2O_3. However, this change was not as significant as changes in the impedance with increasing vol%, further confirming that the predominant factor is the change in conductivity. It should be noted that at the highest frequency range, the imaginary electric modulus shows an additional inclination with increasing frequency. This could potentially be another relaxation process in the sample. Nevertheless, due to the limited observed range, it is not possible to make statements on the cause.

4. Discussion

Conductivity, σ, was determined from the extracted resistance and is plotted in Figure 4. Here, σ increased by orders of magnitude with increasing temperature for the bulk as well as grain boundary values, further confirming that the conduction behavior is a process caused by thermally activated charge carriers [50]. A pronounced increase in conductivity was observed at approximately 410 °C, which is above the Curie point. Similar changes in conductivity in the ferroelectric-to-paraelectric phase transition have been observed in other materials [51,52]. It is also apparent that the conductivity of the grain boundary is higher than that of the bulk, corresponding well to previous investigations on similar NKN-based materials [21]. When adding Al_2O_3 to the material, the conductivities of the bulk and the grain boundary decreased, although this decrease was more pronounced in the grain boundary than in the bulk. For instance, at 360 °C, the decrease is approximately two orders of magnitude for the grain boundary, whereas it is only one order of magnitude for the bulk. The conductivity of NKN with 5 vol% and 15 vol% Al_2O_3 was similar, which is more apparent when comparing all compositions to each other (Figure 4d). A sudden increase in σ from 10 to 15 vol% can be observed. It should be noted that the conductivity can be affected by changes in the microstructure, such as porosity and grain size. To minimize such effects, all samples were prepared with a relative density above 95%. Nonetheless, slight variations cannot be avoided, and they could be responsible for the observed differences. In regard to the grain size, since the average grain size showed a decreasing trend [6], an additional decrease in conductivity should be the result [42]. However, the distribution of Al_2O_3 particles could also impact the conductivity. Depending on the number of agglomerates, the volume of the interface between NKN and Al_2O_3 would change, and by extension, so would the overall conductivity. This could also have implications for the assumptions made by the brick-layer model [25], leading to variations between samples. Considering these points, it is difficult to say whether the significant increase from 10 vol% to 15 vol% is a real effect.

Additionally, the blocking factor β was taken into account. The blocking factor informs about the proportion of the resistance of the grain boundary (R_{gb}) compared to the overall resistance ($R_b + R_{gb}$) and correlates with the fraction of charge carriers blocked at the grain boundaries. The overall conductance is shown in Figure 4d, where, similar to the previously observed conductivities, a decreasing trend is observed. When calculating $\beta = \left(R_{gb}/\left(R_b + R_{gb}\right)\right)$, a continuous decreasing trend from 0.6 to 0.3 with increasing Al_2O_3 content is apparent. These results demonstrate that despite the overall decrease in conductivity, the predominant conduction path shifts more toward the grain boundary.

Since previous observations suggested that the conduction process is thermally activated, the activation energy for these processes can be calculated using the Arrhenius law. The results for the conductivity as a function of temperature as well as the calculated activation energies are shown in Figure 5. Due to significant changes in the conductivity around the Curie point, two separate ranges have been fitted. It should be noted that the activation energy was only estimated below the Curie point, as the number of measurement points was insufficient to obtain reliable results from the fitting. The standard deviation from the linear fitting equations was used to calculate the error. At 0 vol%, the activation energies for the bulk and grain boundary are 0.87 ± 0.06 eV and 1.26 ± 0.09 eV, respectively.

Similar values have been calculated for similar materials and have been linked to the motion of ionized oxygen vacancies [20,41,53]. It should be noted that in oxide ceramics, background impurities are present, leading to intrinsic defects that contribute to the overall concentration of oxygen vacancies [41,54]. In particular, in NKN, the additional volatilization of Na and K can shift the charge balance [53]. In addition, Rafiq et al. have shown that the inclusion of Mn^{2+} ions leads to the substitution of the B-side of the perovskite, which is occupied by Nb^{5+}. Subsequently, the formation of additional oxygen vacancies is favored, leading to a reduction in the activation energy [53]. This reduction was also observed in the grain boundary of the composite material with increasing amounts of Al_2O_3. In view of ionic substitution, Al^{3+} (0.535 A°, CN = 6) most likely replaced Nb^{5+} (0.64 A°, CN = 6) at the B site, resulting in the formation of oxygen vacancies. This is evidenced by the above-discussed behavior of the temperature-dependent permittivity, as well as the formation of a bias field, as shown in a previous study [6]. Similar results were also found in other studies on NKN with Al_2O_3 [9,29]. The activation energy for the bulk response increased from 0.87 ± 0.06 eV to approximately 1.12 ± 0.03 eV, with the most significant change occurring at 5 vol%. As previous studies suggested, the predominant conductive process in NKN is through oxygen vacancy migration at temperatures above 400 °C, with an activation energy between 0.98 and 1.41 [20,55,56]. The findings of the current study correspond well with these values. This suggests that as little as 5 vol% is sufficient to reduce the mobility of oxygen vacancies in the bulk, as was observed in $Ba_{0.85}Ca_{0.15})(Zr_{0.1}Ti_{0.9})O_3/Al_2O_3$ composites [57]. However, whereas in Pb-based perovskite ferroelectrics, a maximum activation energy of 1.2 eV is observed, values for NKN-based can reach up to 1.7 eV [56]. This would suggest that there is an additional mechanism at elevated vol%. It is possible that at higher amounts of Al_2O_3, Al^{3+} diffusion reaches the bulk, thus increasing the number of oxygen vacancies and decreasing the thermal ionization energy. This process would counteract the hindrance of oxygen vacancy migration, resulting in a seemingly unchanging activation energy with additional vol%. On the other hand, the activation energy of the grain boundary decreased from 1.26 ± 0.09 eV to 0.99 ± 0.09 eV, indicating that the diffusion of Al^{3+} into the bulk is limited and predominantly takes place in close vicinity to the grain boundary. This is consistent with the previously mentioned blocking force. As such, Al^{3+} is incorporated at grain boundaries during the sintering of the composites, leading to increased oxygen vacancies. It should be noted that changes in the activation energy can also change if a shift from single-ionized oxygen vacancies (0.3–0.5 eV) to double-ionized oxygen vacancies (0.6–1.2 eV) occurs [58]. Since the measured values are still in the range of double-ionized oxygen vacancies, it seems unlikely that this happened here. When observing the overall conductivity, additional information can be deduced. For one, 15 vol% has a lower overall conductivity than 5 vol%, despite analogous values for the grain and grain boundary. This suggests a variation in the microstructure. Additionally, the overall activation energy remains at approximately 1.08 ± 0.05 eV, since the grain and grain boundary show a counteracting trend with increasing amounts of Al_2O_3. The estimated error is relatively large when compared to the actual values but is still below the actual trend. A further source of variation between the different samples is as previously mentioned, i.e., the microstructure.

Although an increase in the number of oxygen vacancies would increase the conductivity, decreased effective conductivity is observed. For one, as mentioned above, the introduction of Al_2O_3 is similar to increasing the porosity of the sample, which decreases the overall conductivity. However, as previously observed in other materials, an interface can be formed between NKN and Al_2O_3, leading to the formation of oxygen vacancies and an increase in conductivity. Since the effective conductivity decreases, Al_2O_3 seems to have a predominantly decreasing effect.

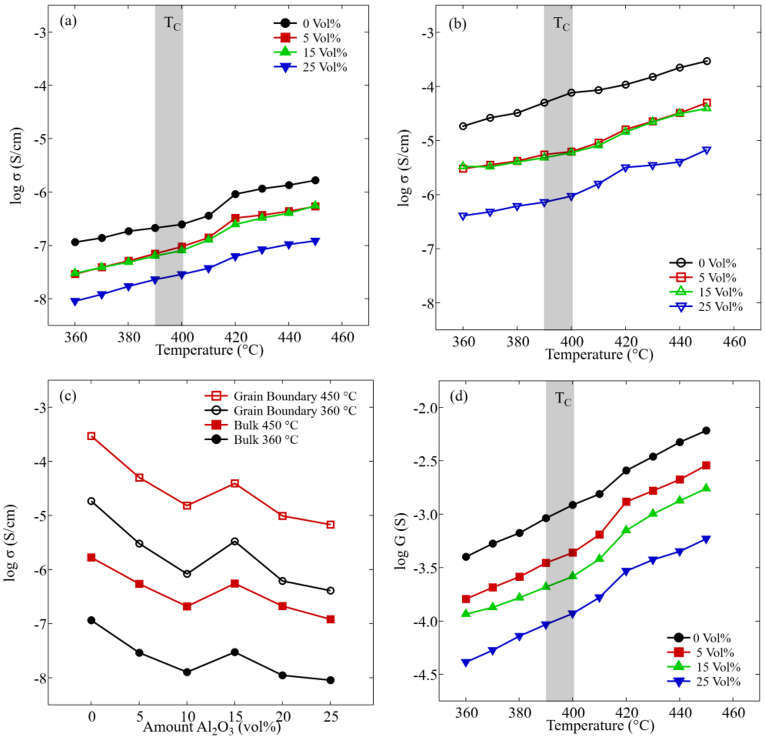

Figure 4. Conductivity of NKN as a function of temperature for bulk (**a**) and grain boundary (**b**), together with the overall conductance G (**d**) at selected vol% Al_2O_3. Gray area shows the phase transition region, which was estimated from permittivity–temperature data. Furthermore, bulk and grain boundary conductivities at 360 °C and 450 °C are shown as a function of Al_2O_3 content (**c**).

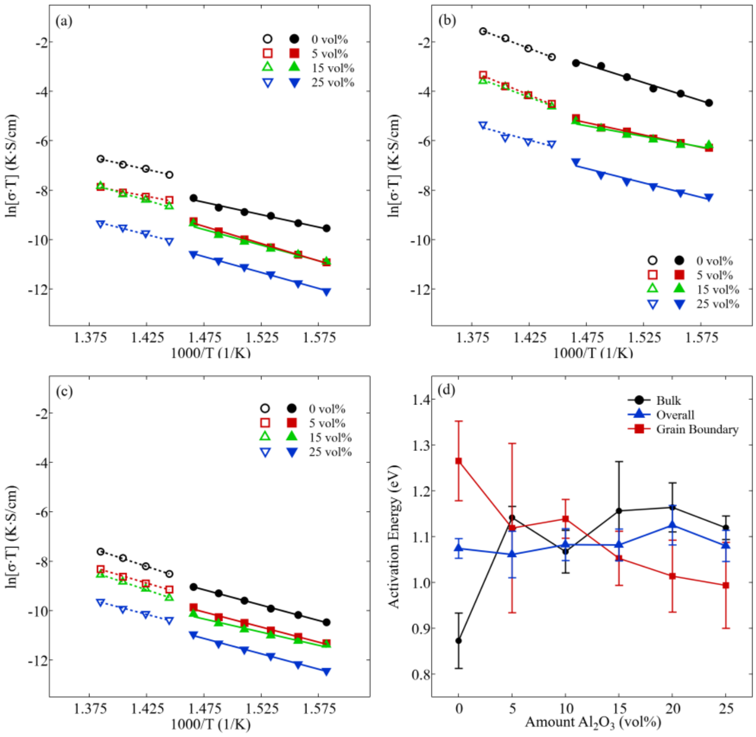

Figure 5. Arrhenius plots of the conductivity for various composites with varying amounts of Al_2O_3 for bulk (**a**), grain boundary (**b**), and overall conductivity (**c**). The activation energies are shown for bulk, grain boundary, and overall in (**d**). Error bars were calculated from the standard deviation given during the fitting process.

5. Conclusions

In this study, 3-0 composites based on NKN with varying Al_2O_3 content were prepared, and their impedance spectra were analyzed at temperatures around the Curie point ($T_C \approx 400$ °C). Nyquist and Bode plots revealed two relaxation processes at approximately 10 Hz and 100–1000 Hz, which were ascribed to the grain boundary and bulk, respectively. The imaginary part of the electric modulus as a function of frequency did not reveal additional relaxation processes, even after the addition of Al_2O_3. The observed spectra were therefore a superimposition of the NKN matrix and Al_2O_3 particles. Since an increase in temperature resulted in a shift of relaxation processes to higher frequencies, the conduction processes were suggested to be thermally activated. Arrhenius plots of the conductivity confirmed this behavior. Furthermore, despite the overall decrease in conductivity, the ratio between the grain boundary and bulk decreased. This suggests predominant conduction through the grain boundary with increasing Al_2O_3. The reason is most likely the diffusion of Al^{3+} into the NKN matrix around the Al_2O_3 particles. This incorporation led to the formation of more oxygen vacancies, which acted as charge carriers. This was confirmed by the changes in activation energies, which increased for the bulk from 0.87± 0.06 eV to approximately 1.12 ± 0.03 eV, whereas the activation energy of the grain boundary decreased from 1.26 ± 0.09 eV to 0.99 ± 0.09 eV. The focus of conductivity is therefore increasingly placed on the grain boundaries between the two materials. Despite this increase in oxygen vacancies, the effective conductivity decreased. A major reason is an opposing effect that occurs with the introduction of low-conductivity Al_2O_3.

Author Contributions: Conceptualization, A.M. and K.-c.K.; methodology, A.M.; formal analysis, A.M.; investigation, A.M.; resources, K.-c.K.; data curation, A.M.; writing—original draft preparation, A.M.; writing—review and editing, K.G.W. and K.-c.K.; visualization, K.G.W. and A.M.; supervision, K.-c.K.; project administration, K.-c.K.; funding acquisition, K.G.W. and K.-c.K. All authors have read and agreed to the published version of the manuscript.

Funding: This research was financially supported by JSPS Grants-in-Aid for Scientific Research B, grant number 22H01773, and NITech research promotion expenses, grant number 2021-wakate-08. K.G.W. gratefully acknowledges financial support for his contributions from the Deutsche Forschungsgemeinschaft under grant GRK2495/F.

Data Availability Statement: The data that support the findings of this study are available within this article.

Acknowledgments: This study was supported by JSPS Japanese-German Graduation Externship, grant number 2019/R1. A. M. would like to thank Jonas Biggemann for the helpful discussions and feedback.

Conflicts of Interest: The authors declare no conflict of interest.

References

1. Rödel, J.; Li, J.F. Lead-Free Piezoceramics: Status and Perspectives. *MRS Bull.* **2018**, *43*, 576–580. [CrossRef]
2. Panda, P.K.; Sahoo, B.; Thejas, T.S.; Krishna, M. High d 33 Lead-Free Piezoceramics: A Review. *J. Electron. Mater.* **2022**, *51*, 938–952. [CrossRef]
3. Lalitha, K.V.; Riemer, L.M.; Koruza, J.; Rödel, J. Hardening of Electromechanical Properties in Piezoceramics Using a Composite Approach. *Appl. Phys. Lett.* **2017**, *111*, 022905. [CrossRef]
4. Song, A.; Liu, Y.; Feng, T.; Li, H.; Zhang, Y.; Wang, X.; Liu, L.; Zhang, B.P.; Li, J.F. Simultaneous Enhancement of Piezoelectricity and Temperature Stability in KNN-Based Lead-Free Ceramics Via Layered Distribution of Dopants. *Adv. Funct. Mater.* **2022**, *32*, 2204385. [CrossRef]
5. Martin, A.; Maier, J.G.; Streich, F.; Kamlah, M.; Webber, K.G. Investigating the Importance of Strain-Coupling in Lead-Free 2–2 Relaxor/Ferroelectric Composites with Digital Image Correlation. *Smart Mater. Struct.* **2022**, *31*, 075009. [CrossRef]
6. Martin, A.; Webber, K.G.; Kakimoto, K. Mechanical and Electrical Properties of $Na_{0.55}K_{0.45}NbO_3$ + 0.2% MnO/Al_2O_3 Composites for Energy Harvesting Applications. *Jpn. J. Appl. Phys.* **2022**, *61*, SN1032. [CrossRef]
7. Yu, Z.D.; Chen, X.M.; Su, Y.L.; Lian, H.L.; Lu, J.B.; Zhou, J.P.; Liu, P. Hot-Press Sintering $K_{0.5}Na_{0.5}NbO_3$–0.5 Mol%Al_2O_3 Ceramics with Enhanced Ferroelectric and Piezoelectric Properties. *J. Mater. Sci.* **2019**, *54*, 13457–13466. [CrossRef]
8. Gao, L.; Zhou, W.; Luo, F.; Zhu, D.; Wang, J. Dielectric and Microwave Absorption Properties of KNN/Al_2O_3 Composite Ceramics. *Ceram. Int.* **2017**, *43*, 12731–12735. [CrossRef]

9. Yang, Z.; Zhu, N.; Ren, W.; Shao, T.; Gao, L.; Zhou, Q.; Yang, Z.; Wang, J.; Qing, Y. Enhanced Microwave Absorption and Electromagnetic Shielding Property of $(1-x)K_{0.5}Na_{0.5}NbO_3$ ~ XAl_2O_3 Nano-Ceramics. *Ceram. Int.* **2020**, *46*, 22738–22744. [CrossRef]
10. Thommerel, E.; Madigou, V.; Villain, S.; Musso, J.; Valmalette, J.C.; Gavarri, J.R. Microstructure Modifications and Modulated Piezoelectric Responses in PLZT/Al_2O_3 Composites. *Mater. Sci. Eng. B* **2003**, *97*, 74–82. [CrossRef]
11. Cao, J.; Yang, Y.; Liang, Y.; Sha, Y.; Li, L.; Zhang, J.; Wang, Y. High Pyroelectric Performance in $Pb_{0.99}Nb_{0.02}[(Zr_{0.57}Sn_{0.43})_{0.94}Ti_{0.06}]_{0{\cdot}98}O_3$/$Al_2O_3$ Composites by Design. *J. Am. Ceram. Soc.* **2022**, *105*, 3331–3338. [CrossRef]
12. Guo, Y.; Kakimoto, K.I.; Ohsato, H. Phase Transitional Behavior and Piezoelectric Properties of $(Na_{0.5}K_{0.5})NbO_3$-$LiNbO_3$ Ceramics. *Appl. Phys. Lett.* **2004**, *85*, 4121–4123. [CrossRef]
13. Tan, L.; Sun, Q.; Wang, Y. Outstanding Piezoelectric Properties of Al-Substituted Potassium-Sodium Niobate-Based Lead-Free Piezoceramics. *J. Alloys Compd.* **2020**, *836*, 155419. [CrossRef]
14. Vendrell, X.; García, J.E.; Bril, X.; Ochoa, D.A.; Mestres, L.; Dezanneau, G. Improving the Functional Properties of $(K_{0.5}Na_{0.5})NbO_3$ Piezoceramics by Acceptor Doping. *J. Eur. Ceram. Soc.* **2015**, *35*, 125–130. [CrossRef]
15. Zhao, Z.; Lv, Y.; Dai, Y.; Zhang, S. Ultrahigh Electro-Strain in Acceptor-Doped KNN Lead-Free Piezoelectric Ceramics via Defect Engineering. *Acta Mater.* **2020**, *200*, 35–41. [CrossRef]
16. Ryu, G.H.; Bowes, P.C.; McGarrahan, J.R.; Irving, D.L.; Dickey, E.C. Fermi Level Pinning in Co-Doped $BaTiO_3$: Part I. DC and AC Electrical Conductivities and Degradation Behavior. *J. Am. Ceram. Soc.* **2022**, *105*, 292–298. [CrossRef]
17. Irvine, J.T.S.; Sinclair, D.C.; West, A.R. Electroceramics: Characterization by Impedance Spectroscopy. *Adv. Mater.* **1990**, *2*, 132–138. [CrossRef]
18. Zeng, Z.; Wu, Q.; Hao, M.; Lu, W.; Fan, G.; Yuchi, M.; Ding, M. Impedance Spectroscopy and Piezoelectric Property of LiF-Doped PZN–PZT Low-Temperature Sintering Piezoelectric Ceramics. *J. Mater. Sci. Mater. Electron.* **2018**, *29*, 8279–8286. [CrossRef]
19. Zhai, Y.; Feng, Y.; Du, J.; Xue, J.; Shen, J.; Lu, Y.; Lu, T.; Fu, P.; Li, W.; Hao, J.; et al. The Impedance, Dielectric and Piezoelectric Properties of Tb_4O_7 and Tm_2O_3 Doped KNN Ceramics. *J. Mater. Sci. Mater. Electron.* **2019**, *30*, 4352–4358. [CrossRef]
20. Nishiyama, H.; Kakimoto, K.I.; Hatano, K.; Kishimoto, S.; Sasaki, N. Cyclic Properties and Impedance Analysis of $(Li,Na,K)NbO_3$-Based Multilayered Piezoceramics. *Jpn. J. Appl. Phys.* **2020**, *59*, SPPD05. [CrossRef]
21. Kamal, A.; Rafiq, M.A.; Rafiq, M.N.; Usman, M.; Waqar, M.; Anwar, M.S. Structural and Impedance Spectroscopic Studies of CuO-Doped $(K_{0.5}Na_{0.5}Nb_{0.995}Mn_{0.005}O_3)$ Lead-Free Piezoelectric Ceramics. *Appl. Phys. A Mater. Sci. Process.* **2016**, *122*, 1–10. [CrossRef]
22. Newnham, R.E.; Skinner, D.P.; Cross, L.E. Connectivity and Piezoelectric-Pyroelectric Composites. *Mater. Res. Bull.* **1978**, *13*, 525–536. [CrossRef]
23. Zhang, H.; Mak, C.L. Impedance Spectroscopic Characterization of Fine-Grained Magnetoelectric $Pb(Zr_{0.53}Ti_{0.47})O_3$-$(Ni_{0.5}Zn_{0.5})Fe_2O_4$ Ceramic Composites. *J. Alloys Compd.* **2012**, *513*, 165–171. [CrossRef]
24. Ahmed, S.; Atif, M.; Nadeem, M.; Ali, Z.; Khalid, W.; Nasir Khan, M. Impedance Spectroscopy and Conduction Mechanism of Ferroelectric Rich $PbZr_{0.52}Ti_{0.48}O_3-CoFe_2O_4$ Magnetoelectric Composite. *Ceram. Int.* **2020**, *46*, 21090–21096. [CrossRef]
25. Fleig, J.; Maier, J. The Impedance of Ceramics with Highly Resistive Grain Boundaries: Validity and Limits of the Brick Layer Model. *J. Eur. Ceram. Soc.* **1999**, *19*, 693–696. [CrossRef]
26. Fisher, J.G.; Rout, D.; Moon, K.S.; Kang, S.J.L. High-Temperature X-Ray Diffraction and Raman Spectroscopy Study of $(K_{0.5}Na_{0.5})NbO_3$ Ceramics Sintered in Oxidizing and Reducing Atmospheres. *Mater. Chem. Phys.* **2010**, *120*, 263–271. [CrossRef]
27. Fisher, J.G.; Rout, D.; Moon, K.S.; Kang, S.J.L. Structural Changes in Potassium Sodium Niobate Ceramics Sintered in Different Atmospheres. *J. Alloys Compd.* **2009**, *479*, 467–472. [CrossRef]
28. Masó, N.; Beltrán, H.; Cordoncillo, E.; Escribano, P.; West, A.R. Electrical Properties of Fe-Doped $BaTiO_3$. *J. Mater. Chem.* **2006**, *16*, 1626–1633. [CrossRef]
29. Cheng, Y.; Xing, J.; Wang, T.; Wang, F.; Li, R.; Sun, X.; Xie, L.; Tan, Z.; Zhu, J. Realization of Densified Microstructure and Large Piezoelectricity in KNN Ceramics via the Addition of Oxide Additives. *J. Mater. Sci. Mater. Electron.* **2021**, *32*, 20211–20224. [CrossRef]
30. Huo, S.; Yuan, S.; Tian, Z.; Wang, C.; Qiu, Y. Grain Size Effects on the Ferroelectric and Piezoelectric Properties of $Na_{0.5}K_{0.5}NbO_3$ Ceramics Prepared by Pechini Method. *J. Am. Ceram. Soc.* **2012**, *95*, 1383–1387. [CrossRef]
31. Jaffe, H.; Berlincourt, D.; McKee, J.M. Effect of Pressure on the Curie Temperature of Polycrystalline Ceramic Barium Titanate. *Phys. Rev.* **1957**, *105*, 57. [CrossRef]
32. Samara, G.A. Pressure and Temperature Dependences of the Dielectric Properties of the Perovskites $BaTiO_3$ and $SrTiO_3$. *Phys. Rev.* **1966**, *151*, 378–386. [CrossRef]
33. Martin, A.; Webber, K.G.; Khansur, N.H.; Eckstein, U.; Riess, K.; Kakimoto, K. High Temperature Piezoelectric Response of Polycrystalline Li-Doped (K, Na) NbO 3 Ceramics under Compressive Stress. *J. Appl. Phys.* **2020**, *127*, 114101. [CrossRef]
34. Alford, N.M.; Penn, S.J. Sintered Alumina with Low Dielectric Loss. *J. Appl. Phys.* **1998**, *80*, 5895. [CrossRef]
35. Schader, F.H.; Aulbach, E.; Webber, K.G.; Rossetti, G.A. Influence of Uniaxial Stress on the Ferroelectric-to-Paraelectric Phase Change in Barium Titanate. *J. Appl. Phys.* **2013**, *113*, 174103. [CrossRef]
36. Uchino, K.; Nomura, S. Critical Exponents of the Dielectric Constants in Diffused-Phase-Transition Crystals. *Ferroelectrics* **1982**, *44*, 55–61. [CrossRef]

37. Samara, G.A. Pressure and Temperature Dependence of the Dielectric Properties and Phase Transitions of the Ferroelectric Perovskites: PbTiO3 and BaTiO3. *Ferroelectrics* **1971**, *2*, 277–289. [CrossRef]
38. Zhang, L.; Zhong, W.L.; Wang, C.L.; Zhang, P.L.; Wang, Y.G. Dielectric Properties of $Ba_{0.7}Sr_{0.3}TiO_3$ Ceramis with Different Grain Size. *Phys. Status Solidi* **1998**, *543*, 543–548. [CrossRef]
39. Zhao, Z.; Buscaglia, V.; Viviani, M.; Buscaglia, M.T.; Mitoseriu, L.; Testino, A.; Nygren, M.; Johnsson, M.; Nanni, P. Grain-Size Effects on the Ferroelectric Behavior of Dense Nanocrystalline $BaTiO_3$ Ceramics. *Phys. Rev. B-Condens. Matter Mater. Phys.* **2004**, *70*, 1–8. [CrossRef]
40. Li, S.B.; Wang, C.B.; Li, L.; Shen, Q.; Zhang, L.M. Effect of Annealing Temperature on Structural and Electrical Properties of BCZT Ceramics Prepared by Plasma Activated Sintering. *J. Alloys Compd.* **2018**, *730*, 182–190. [CrossRef]
41. Hussain, F.; Sterianou, I.; Khesro, A.; Sinclair, D.C.; Reaney, I.M. P-Type/n-Type Behaviour and Functional Properties of $K_xNa_{(1-x)}NbO_3$ ($0.49 \leq x \leq 0.51$) Sintered in Air and N_2. *J. Eur. Ceram. Soc.* **2018**, *38*, 3118–3126. [CrossRef]
42. Wang, X.; Huan, Y.; Zhao, P.; Liu, X.; Wei, T.; Zhang, Q.; Wang, X. Optimizing the Grain Size and Grain Boundary Morphology of (K,Na)NbO_3-Based Ceramics: Paving the Way for Ultrahigh Energy Storage Capacitors. *J. Mater.* **2021**, *7*, 780–789. [CrossRef]
43. Brailsford, A.D.; Hohnke, D.K. The Electrical Characterization of Ceramic Oxides. *Solid State Ion.* **1983**, *11*, 133–142. [CrossRef]
44. Feighery, A.J.; Irvine, J.T.S. Effect of Alumina Additions upon Electrical Properties of 8 Mol.% Yttria-Stabilised Zirconia. *Solid State Ion.* **1999**, *121*, 209–216. [CrossRef]
45. Yang, F.; Zhao, X.; Xiao, P. Electrical Properties of YSZ/Al_2O_3 Composite and YSZ/Al_2O_3 Interface Studied by Impedance Spectroscopy and Finite Element Modelling. *Solid State Ion.* **2010**, *181*, 783–789. [CrossRef]
46. Morrison, F.D.; Sinclair, D.C.; West, A.R. Characterization of Lanthanum-Doped Barium Titanate Ceramics Using Impedance Spectroscopy. *J. Am. Ceram. Soc.* **2001**, *84*, 531–538. [CrossRef]
47. Bagum, A.; Hossen, M.B.; Chowdhury, F.U.Z. Complex Impedance and Electric Modulus Studies of Al Substituted $Co_{0.4}Cu_{0.2}Zn_{0.4}Al\ XFe_2\text{-}XO_4$ Ferrites Prepared by Auto Combustion Technique. *Ferroelectrics* **2016**, *494*, 19–32. [CrossRef]
48. Belal Hossen, M.; Akther Hossain, A.K.M. Complex Impedance and Electric Modulus Studies of Magnetic Ceramic $Ni_{0.27}Cu_{0.10}Zn_{0.63}Fe_2O_4$. *J. Adv. Ceram.* **2015**, *4*, 217–225. [CrossRef]
49. Wang, X.; Huan, Y.; Wang, Z.; Lin, X.; Huang, S.; Wei, T.; Li, L.; Wang, X. Electrical Conduction and Dielectric Relaxation Mechanisms in the KNN-Based Ceramics. *J. Appl. Phys.* **2019**, *126*, 104101. [CrossRef]
50. Molak, A.; Ksepko, E.; Gruszka, I.; Ratuszna, A.; Paluch, M.; Ujma, Z. Electric Permittivity and Conductivity of $(Na_{0.5}Pb_{0.5})(Mn_{0.5}Nb_{0.5})O_3$ Ceramics. *Solid State Ion.* **2005**, *176*, 1439–1447. [CrossRef]
51. Portelles, J.; Almodovar, N.S.; Fuentes, J.; Raymond, O.; Heiras, J.; Siqueiros, J.M. Ac Conductivity in Gd Doped $Pb(Zr_{0.53}Ti_{0.47})O_3$ Ceramics. *J. Appl. Phys.* **2008**, *104*, 073511. [CrossRef]
52. Tsai, C.C.; Chu, S.Y.; Hong, C.S.; Chen, S.F. Effects of ZnO on the Dielectric, Conductive and Piezoelectric Properties of Low-Temperature-Sintered PMnN-PZT Based Hard Piezoelectric Ceramics. *J. Eur. Ceram. Soc.* **2011**, *31*, 2013–2022. [CrossRef]
53. Rafiq, M.A.; Tkach, A.; Costa, M.E.; Vilarinho, P.M. Defects and Charge Transport in Mn-Doped $K_{0.5}Na_{0.5}NbO_3$ Ceramics. *Phys. Chem. Chem. Phys.* **2015**, *17*, 24403–24411. [CrossRef] [PubMed]
54. Bowes, P.C.; Baker, J.N.; Harris, J.S.; Behrhorst, B.D.; Irving, D.L. Influence of Impurities on the High Temperature Conductivity of $SrTiO_3$. *Appl. Phys. Lett.* **2018**, *112*, 022902. [CrossRef]
55. Liu, L.; Fan, H.; Fang, L.; Chen, X.; Dammak, H.; Thi, M.P. Effects of Na/K Evaporation on Electrical Properties and Intrinsic Defects in $Na_{0.5}K_{0.5}NbO_3$ Ceramics. *Mater. Chem. Phys.* **2009**, *117*, 138–141. [CrossRef]
56. Rani, R.; Sharma, S.; Rai, R.; Kholkin, A.L. Investigation of Dielectric and Electrical Properties of Mn Doped Sodium Potassium Niobate Ceramic System Using Impedance Spectroscopy. *J. Appl. Phys.* **2011**, *110*, 104102. [CrossRef]
57. Yan, X.; Zheng, M.; Zhu, M.; Hou, Y. Enhanced Electrical Resistivity and Mechanical Properties in BCTZ-Based Composite Ceramic. *J. Adv. Dielectr.* **2019**, *9*, 1950036. [CrossRef]
58. Peláiz-Barranco, A.; Guerra, J.D.S. Dielectric Relaxation Related to Single-Ionized Oxygen Vacancies in $(Pb_{1-x}La_x)(Zr_{0.90}Ti_{0.10})_{1-x}/4O_3$ Ceramics. *Mater. Res. Bull.* **2010**, *45*, 1311–1313. [CrossRef]